Journal of Molecular Liquids 389 (2023) 122872

Contents lists available at ScienceDirect

Journal of Molecular Liquids

journal homepage: www.elsevier.com/locate/molliq

Removal of lead (II) from aqueous solution using epichlorohydrin cross-linked shrimp waste-derived chitosan based @ calcium phosphates biocomposite: Experimental study and computational approach

Rachid El Kaim Billah [a,b], Selçuk Şimşek [c,*], Hicham Majdoubi [d], Savaş Kaya [e], Mahfoud Agunaou [a], Abdessadik Soufiane [a], Konstantin P. Katin [f]

[a] Department of Chemistry, University of Chouaïb Doukkali, Faculty of Sciences, Laboratory of Coordination and Analytical Chemistry, Avenue Jabran Khalil Jabran B.P 299-24000, El Jadida, Morocco
[b] Science Engineer Laboratory for Energy, ENSAJ, Chouaïb Doukkali University, El Jadida, Morocco
[c] Sivas Cumhuriyet University, Faculty of Science, Department of Chemistry, 58140 Sivas, Turkey
[d] Materials Science Energy and Nanoengineering Department, Mohamed VI Polytechnic University, Benguerir, Morocco
[e] Sivas Cumhuriyet University, Health Services Vocational School, Department of Pharmacy, 58140 Sivas, Turkey
[f] Institute of Nanoengineering in Electronics, Spintronics and Photonics, National Research Nuclear University "MEPhI", Kashirskoe Shosse 31, Moscow 115409, Russia

A B S T R A C T

An economical composite has been synthesized utilizing chitosan derived from discarded shrimp shells and hydroxyapatite extracted from waste bovine bones. This research delves into the composite's adsorption properties for the purpose of eliminating Pb ions from wastewater. The structure of this novel composite has been meticulously examined through techniques including scanning electron microscopy (SEM), Fourier transform infrared spectroscopy (FTIR), X-ray diffraction (XRD), thermogravimetric analysis (TGA), and Brunauer–Emmett–Teller (BET) analyses. Factors such as concentration, time, temperature, adsorbent dosage, and pH have been scrutinized to understand their impacts on lead ion adsorption. Concurrently, relevant adsorption parameters have been ascertained. Notably, the adsorption capacity, as determined by the Langmuir model, was found to be 154.88 mgg^{-1}. To elucidate the adsorption kinetics, the PSO and IP models were employed. The adsorption enthalpy exhibited a positive value, while the free enthalpy displayed negativity. The mechanism governing adsorption was expounded upon through theoretical calculations, which concurred with and validated the experimental results.

1. Introduction

In recent times, the escalation in industrial production has led to the contamination of the environment and water sources with a multitude of wastes. These wastes encompass dyes, organic pollutants, and metals like lead, mercury, and uranium. Notably, lead finds extensive application in various domains, particularly in dyes and batteries. Regrettably, its pervasive usage carries severe implications for human health due to its manifold detrimental effects.

Lead, existing predominantly in the form of Pb (II) within aqueous solutions, has been unequivocally demonstrated to exhibit toxicity toward several organs, with the most notable impact on bone marrow, blood, the central nervous system, and the kidneys. It is noteworthy that even at minute blood concentrations, less than 3.5 μg dL^{-1}, children have exhibited distressing issues such as mental retardation and learning disabilities [1,2].

The imperative to eliminate lead from the human ecosystem has grown significantly, given its diverse pathways of entry, particularly through sources like drinking water and air. Addressing this concern has become paramount to safeguarding public health.

The removal of pollutants from aqueous media presents a significant challenge. While various physicochemical and biological treatment methods exist, a majority of them are deemed unfavorable due to their lack of sustainability and economic viability. Notably, when it comes to metallic pollutants, a primary issue arises from the inability to effectively employ removal techniques at low concentrations. In this context, adsorption emerges as a robust approach for eliminating pollutants via solid-phase interactions, finding extensive application across diverse domains. Historical records reveal the utilization of adsorbents such as carbon, clay, and zeolite for adsorption processes, encompassing tasks ranging from alleviating unpleasant odors in the air to purifying contaminated water sources [3]. Advancements in technology have ushered in innovative designs of adsorbents, including polymers [4], MOFs (Metal-Organic Frameworks) [5], and composite materials [6].

* Corresponding author.
E-mail address: simsek@cumhuriyet.edu.tr (S. Şimşek).

https://doi.org/10.1016/j.molliq.2023.122872
Received 18 April 2023; Received in revised form 17 August 2023; Accepted 18 August 2023
Available online 20 August 2023

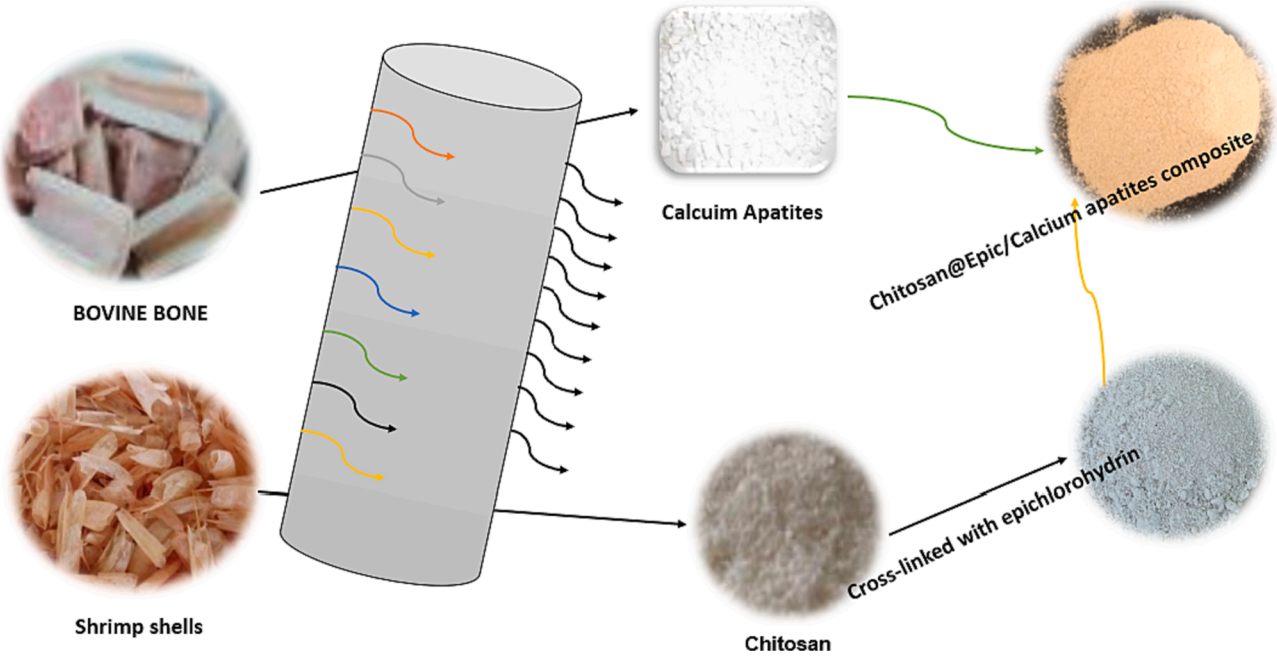

Fig. 1. Schematic demonstration of the preparation steps of Shrimp waste-derived chitosan Based @ Calcuim Apatites Biocomposite.

However, it remains pertinent to acknowledge that natural materials continue to stand out as preferred adsorbents due to their economic viability and wide availability.

Chitosan, a naturally abundant polymer, finds notable utility in adsorption studies not in its pristine form, but through its extensively utilized modified structures and composites. The selection of chitosan as an adsorbent material is grounded in its profusion of hydroxyl groups, which confer remarkable hydration properties. Additionally, the amine functionalities of chitosan play a pivotal role, enabling both physical modifications such as solubilization and shaping, as well as chemical modifications such as grafting reactive groups and crosslinking [7]. Chitosan-based adsorbents have gained widespread prominence in the realm of metal removal investigations, primarily attributed to their inherent ability for facile chelation with metals [8]. Nevertheless, it's essential to acknowledge that chitosan cannot function as a standalone adsorbent material due to its vulnerability to dissolution under acidic conditions.

Hydroxyapatite (Hap), a phosphate-based framework inherent in the rigid components of biological entities like bones, holds a favored status within the realm of adsorption investigations [9]. We chose to use natural Hap because it constitutes the mineral matrix of calcified tissues, that is bones and teeth (it is used as a coating for prostheses). Hap is also known for its heavy metal-trapping properties; it is highly reactive and has interesting trapping capacities [10].

The primary aim of this investigation was to fabricate a biocomposite employing two naturally occurring components, chitosan and calcium phosphate, to serve as efficient adsorbents for Pb (II) ions. Chitosan, derived from discarded shrimp waste, was isolated to yield a biodegradable and non-toxic adsorbent derived from abundant natural resources. The ensuing chitosan was subsequently enhanced through modification with calcium phosphate (Hap), sourced from bovine bones, resulting in the creation of an economical biocomposite. Consequently, the focus of this study was directed toward the extraction of lead, a pollutant metal, from wastewater through its adsorption onto the aforementioned composite. This composite material, constituted from elements readily procured from biomass and subsequently disposed of as waste, was subjected to rigorous investigation. Characterization of the synthesized material was carried out employing FTIR, SEM, and XRD techniques. Within the scope of this study, an exhaustive analysis of diverse parameters impacting adsorption was conducted, leading to the comprehensive determination of all pertinent adsorption-related factors.

2. Experimental

2.1. Chemical and reagents

The chemicals and reagents employed in this research were sourced at analytical reagent (A.R) grade, or as explicitly listed. Lead nitrate ($Pb(NO_3)_2$) at a concentration of 1 gL^{-1}, with a purity of ≥99 % (Sigma-Aldrich), was utilized as the primary Pb (II) source. A stock solution of Pb (II) at 1000 mg L^{-1} was meticulously prepared by dissolving precise quantities of Pb (NO3)2 in doubly-distilled water. Sodium hydroxide (NaOH), with a purity surpassing 99 %, and analytical grade hydrochloric acid (HCl, 2N), were procured from Sigma-Aldrich to facilitate pH adjustments of the solution. Throughout the experiments, double-distilled water was employed. Furthermore, nitric acid (HNO_3, 0.1 N), magnesium nitrate (Mg (NO_3), 98 %), sodium nitrate ($NaNO_3$, 99 %), copper (II) nitrate trihydrate ($Cu(NO_3)_2{\cdot}3H_2O$, 99 %), zinc nitrate hexahydrate (Cu (NO_3)2··$6H_2O$, 98 %), hydrochloric acid (HCl, 0.1 N), anhydrous sodium sulfate (Na_2SO_4, 99 %), sodium chloride (NaCl), sulfuric acid (H_2SO_4), acetic acid (CH_3COOH), and ethanol (C_2H_5OH) were all procured from Sigma-Aldrich in Germany.

2.2. Preparation of adsorbents

2.2.1. Preparation of chitin

Chitin is derived from shrimp shells collected from the El-Jadida region in Morocco. This process involves two distinct stages: demineralization and deproteinization.

During the demineralization stage, an HCl solution (2N) with a mass-to-volume ratio of 1:40 is employed at room temperature. The resulting mixture is vigorously stirred for a duration of 12 h. Subsequently, the obtained product is subjected to washing with distilled water until achieving a neutral pH, followed by drying for 24 h at 50 °C.

For the deproteinization step, a 10 % NaOH solution (mass-to-volume ratio of 1:20) is utilized, and the process is conducted at 80 °C under reflux conditions with continuous stirring for a period of 12 h. The

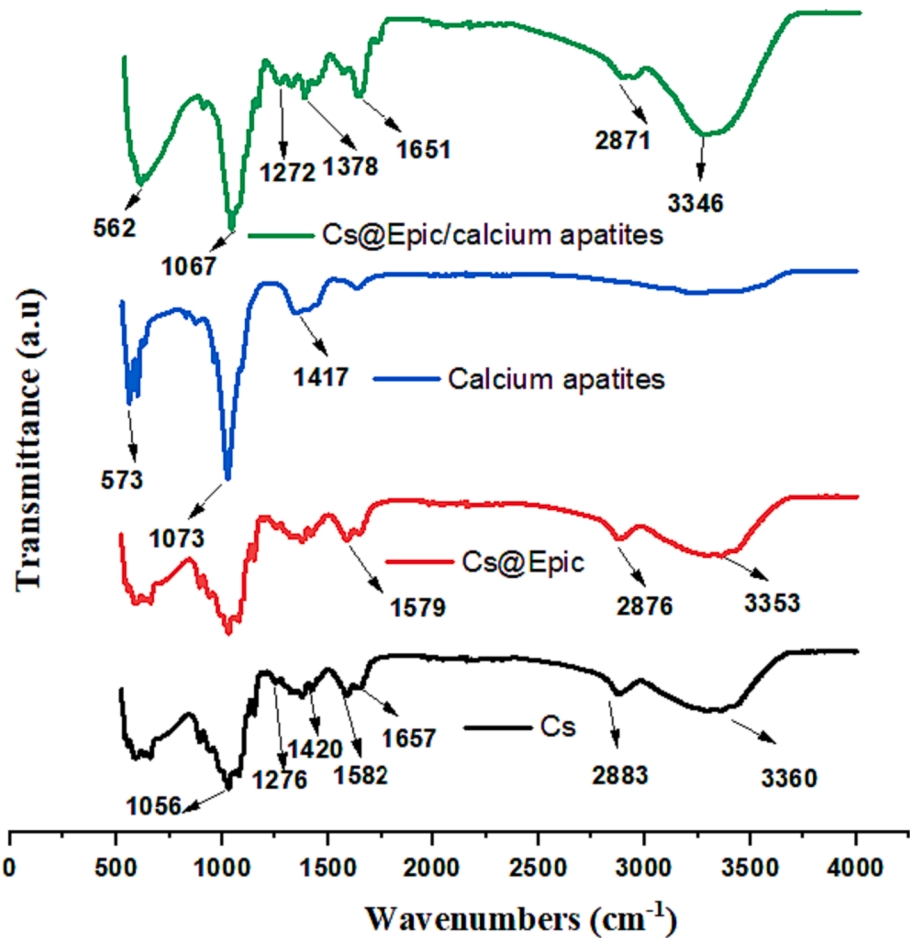

Fig. 2. FTIR of Cs, Cs@Epic, Calcium apatites and Cs@Epi/Calcium apatites.

resultant chitin is separated through filtration, followed by washing with distilled water to attain a neutral pH. The final step involves drying the chitin at 50 °C for 24 h.

The production of chitosan entails the deacetylation of chitin, involving the removal of acetyl groups to yield chitosan. The underlying principle of this procedure is to place the previously prepared chitin within a flask containing crushed NaOH (50 %) and then subjecting the mixture to reflux at 100 °C for 10 h with continuous stirring.

2.2.2. Preparation of calcium phosphates

Calcium apatite was extracted from bovine bones. The bones were initially cleaned using a mixture of water and bleach, followed by air-drying. Subsequently, the bones were cut into small pieces and subjected to a torch treatment to eliminate undesired components like bone marrow. The remaining fragments were further ground into a powder using a mortar, and then calcined for 3 h at a temperature of 800 °C. Pellets were formed by compacting the bone powder using a hydraulic press and subsequently positioned within an alumina crucible for heat treatment at 1000 °C for a duration of 2 h.

2.2.3. Preparation of chitosan cross-linked with epichlorohydrin @Hap

The cross-linked chitosan was prepared as depicted in (Fig. 1). Initially, 4 g of chitosan was dissolved in 150 ml of a 1 % (v/v) acetic acid solution. Subsequently, a cross-linking agent consisting of 0.1 M epichlorohydrin and sodium hydroxide NaOH with a molarity of 0.067 M was introduced. The mixture was stirred for 24 h, after which 2 g of calcium apatite powder was gradually incorporated into the crosslinked chitosan solution. This mixture was stirred for an additional 12 h. Finally, the composite was subjected to oven-drying at 80 °C.

2.3. Adsorption experiments

The Pb(II) adsorption experiments were conducted using a discontinuous system. The adsorption tests were performed in 250 ml glass beakers, where 50 ml of Pb(II) solutions were transferred from 200 ml beakers containing Cs@Epic/Calcium apatite. The stirring was kept constant during the experiments, and the relevant experimental parameters were maintained. Various experimental parameters were investigated, including pH (ranging from 2 to 7, time = 2 h, C_o: 100 mg/L, and T = 25 °C), adsorbent mass (m: 0.01–0.2 g, Co: 100 mg/L, time = 2 h, pH = 5, and T = 25 °C), contact time (t: 5–360 min, Co: 100 mg/L, pH = 5, and T = 25 °C), as well as the initial chromium concentration's impact on the adsorption process (Co: 25–500 mg/L, pH = 5, time = 2 h, and T = 25 °C). The initial pH of the solution was adjusted using either 0.1 M HCl or 0.1 M NaOH.

The remaining concentration of samples was determined through inductively coupled plasma-atomic emission spectrometry (Thermo Jarrell Ash Corporation Atom Scan 16, Williamston, SC, USA). The adsorption capacity (qt in mg/g) and adsorption percentage (% Removal) at specific contact times were computed using the following equations:

$$q_t = \frac{(C_o - C_t)V}{m} \quad (1)$$

$$\%Removal = \frac{(C_o - C_t)}{C_o} \times 100 \quad (2)$$

Where C_o and C_t are the amounts of initial and retained Pb (II) in the solution at time t (mgL^{-1}), respectively. V is the solution volume (L) and

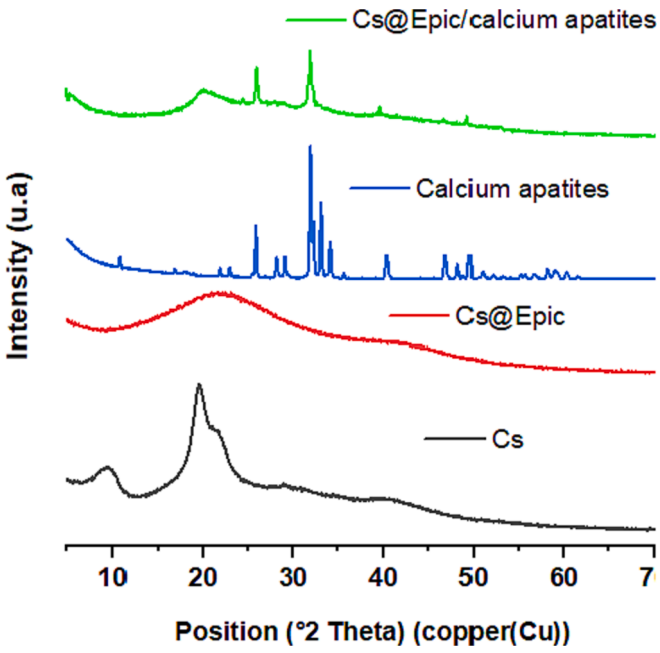

Fig. 3. XRD of Cs,Cs@Epic, Calcium apatites and Cs@Epic/Calcium apatites.

m is the mass of adsorbent (g). All experimental studies was repeated two times.

2.4. Characterizations

Fourier-transform infrared (FT-IR) spectroscopy (Thermo-scientific Spectrometer) was utilized to identify active functional groups present on the composite surface. X-ray diffraction (XRD) analysis was performed using a Bruker D8 diffractometer operating at 45 kV/100 mA, employing CuKα radiation with a Ni filter. The surface morphology of the samples was examined via scanning electron microscopy (SEM-EDX) using a Philips XL 30 ESEM (Accelerating voltage: 20.00 kV). BET analysis was conducted using the ASAP 2020 equipment from Micromeritics, Norcross, GA, USA. The adsorption isotherm was constructed by obtaining relative pressure and adsorption quantity data at 77 K. The samples were degassed at 573 K for 24 h under vacuum before analysis. The final pH of each supernatant was measured using the inoLab® pH 7310 pH meter from Xylem Analytics.

3. Results and discussion

3.1. Characterization

3.1.1. FTIR

The infrared spectra of Cs, Cs@Epic and Cs@Epic/Calcium apatites were determined by Fourier Transform Infrared Spectroscopy (FTIR) and given in Fig. 2. The spectrum of chitosan (Cs), showed peaks at 3360 cm^{-1} due to the overlap of the O—H and N—H stretching bands which is related to extra-molecular hydrogen bonding, 2883 cm^{-1} for the aliphatic C—H stretch, 1582 cm^{-1} for N—H bending (amide II) [11], 1657 cm^{-1} for the deformation of C═O (amide I) indicating the partially acetylated form of chitin, 1420 and 1378 cm^{-1} for the deformation of C—H, 1276 cm^{-1} for C—N (amide II), 1148 cm^{-1}, 1056 cm^{-1} and 1037 cm^{-1} for C—O—C stretching (asymmetric stretching of the C—O—C bridge), (skeletal vibration creating CO stretching) are characteristic of glucosamine residues in chitosan [12,13]. As shown in the Cs@Epic figure, a drop in intensity at 3400 cm^{-1} is observed indicating the chitosan OH group interaction with Cs@Epic [14]. Additionally, a decrease in intensity at 1500–1700 cm^{-1} indicates the interaction of the chitosan N—H group with Cs@Epic. The IR spectrum of Calcium phosphate powder confirms the formation of Hap which contains P—O and O—H bands of the phosphate and hydroxyl groups which are constituents of phosphate. The corresponding bands of the vibrational mode v3 of the PO_4^{3-} tetrahydric ions, symmetric elongation vibration v4 of the PO_4^{3-} ions, and the vibration frequencies of the carbonate groups CO_3^{2-} are observed at 1073 cm^{-1}, 565 cm^{-1}, and 1417 cm^{-1} respectively [6,15]. The Powders IR spectra are mainly characterized by the bands associated with an appetite structure. FTIR spectrum of Cs@Epic/Calcium apatites, the apatite absorption bands (at 562 and 1067 cm^{-1}) are observed in the composite, also the Cs bands corresponding to the amide group: the vibration of C═O (amide I) (1651 cm^{-1}), N—H (amide II) (1649 cm^{-1}), CN (amide III) (1272 cm^{-1}), and C—H (881 cm^{-1}), changed their initial position towards low frequencies, this can be explained by the ionic interaction between the positively charged amino groups of the Cs@Epic and the negatively charged groups of the phosphate.

3.1.2. XRD

The chitosan diffractogram (Fig. 3) shows characteristic peaks at the 2θ position at 10.16°, and 19.46° corresponding to a polymorph of chitosan, which is already reported in the literature as a polymorph [16,17]. The diffractogram (Cs@Epic) indicates that the peaks established at 2θ = 9°, and 20° became broad with a strong decrease in their intensity. These changes imply that the alignment of the chitosan chain after cross-linking with epichlorohydrin became more disordered, making the chitosan more amorphous [18]. These changes brought that the cross-linking of chitosan was carried out correctly. The diffractogram of Calcium apatites shows the presence of the rays at the positions 2Θ: 25. 87∘, 28.10, 29.03, 31.76, 32.16, 33.01, 34.08, 39.25, 46.65, 48.54, and 49.58, based on the sheet (date from JCPDS file, no. 90-432), they correspond to the planes (0 0 2), (1 0 2),(2 1 0), (2 1 1),(1 1 2), (3 0 0), (2 0 2),(3 1 0), (2 2 2), (2 1 2) and (2 1 3) respectively [19] in good agreement with the XRD model of a standard Hap. The XRD model of Cs@Epic/Calcium apatites shows the main characteristic peaks of calcium apatites observed at the angle 2 = 30.15°, 32.16° and 48.54° with a decrease in the intensity of cross-linked Cs. These results highlight the interaction between chitosan and Calcium apatites.

3.1.3. SEM-EDX

SEM scanning electron microscopy analysis of Cs Cs@Epic (a) and Cs@Epic/Calcium apatite (b) are shown in Fig. 4. Cs@Epic exhibited a smooth and flat surface, while in the Cs@Epic/Calcium Apatite composite the original flat structure of chitosan has been destroyed to form a rough surface, showing the presence of Calcium Apatite on the entire surface of the Cs@Epic/Calcium Apatite composite, the surface is denser with the particles grainy, this may be due to the interaction of chitosan with Apatite particles. The presence of calcium phosphate in the biocomposite was confirmed with energy-dispersive X-ray spectroscopy (EDX). EDX analysis of the adsorbent is shown in Fig. 4. As can be seen, the existence of P and Ca is proven in the composite, and also, the Calcium Apatites particles are evenly distributed over the cross-linked chitosan.

3.1.4. BET

The analysis of the N_2 adsorption/desorption isotherm curves for the bio-composites Cs@Epic and Cs@Epic/Calcium apatites is presented in Fig. 5. The isotherms of the three studied materials were consistent with a type IV isotherm, exhibiting H3 hysteresis loop behavior [20]. This suggests that both Cs@Epic and Cs@Epic/Calcium apatites possess mesopores capable of undergoing capillary condensation [21]. Furthermore, when comparing Cs@Epic, which has a specific surface area (SSA) of 3.2 m^2/g, to Cs@Epic/Calcium apatites, it becomes evident that the latter has a significantly higher SSA (approximately five times greater, at 15.3 m^2/g). This result confirms that the incorporation of calcium apatites has indeed enhanced the porous structure of the resulting composite material.

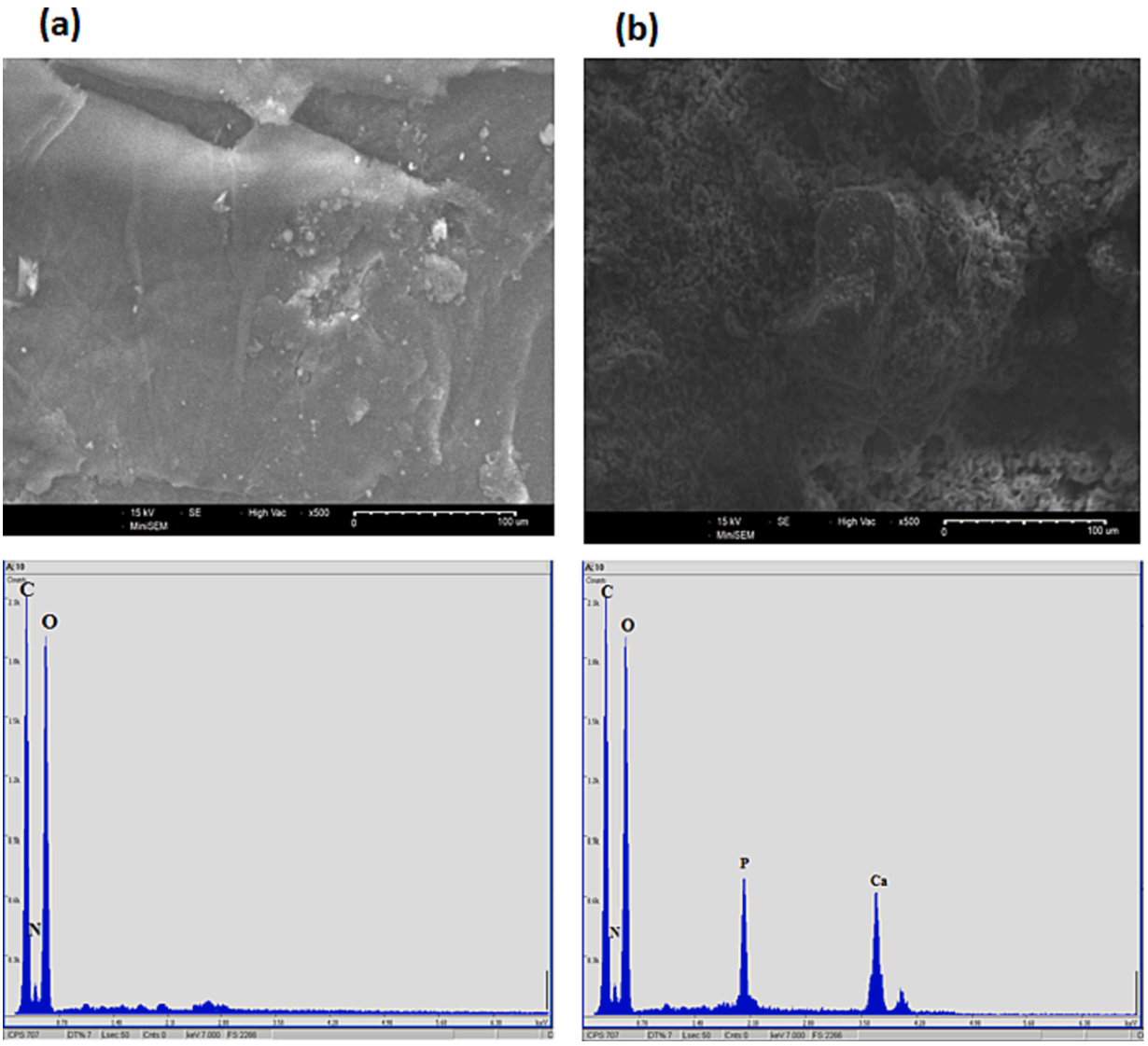

Fig. 4. SEM images and EDX analysis of (a) Cs@Epic et (b) du Cs@Epic/Calcuim apatites.

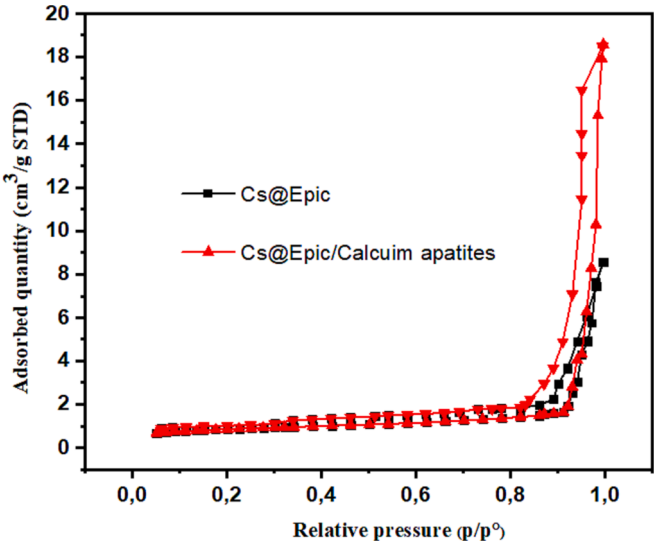

Fig. 5. The N_2 adsorption–desorption isotherms Cs@Epic and du Cs@Epic/ Calcium apatites.

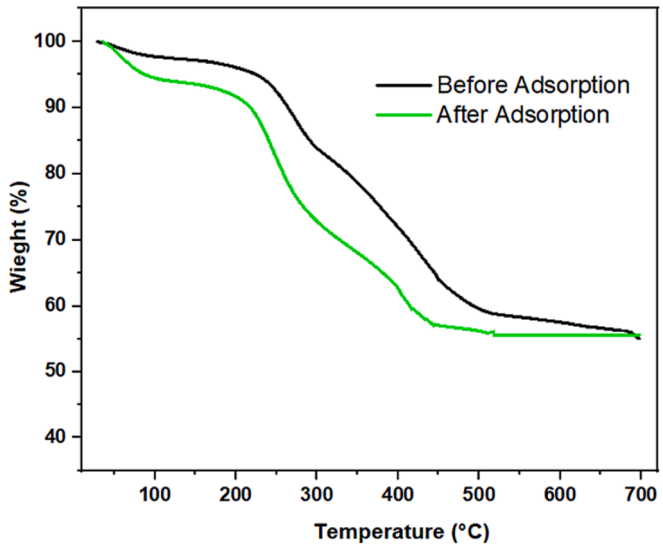

Fig. 6. TGA curves of the Cs@Epic/Calcium appetites before and after Pb (II) adsorption.

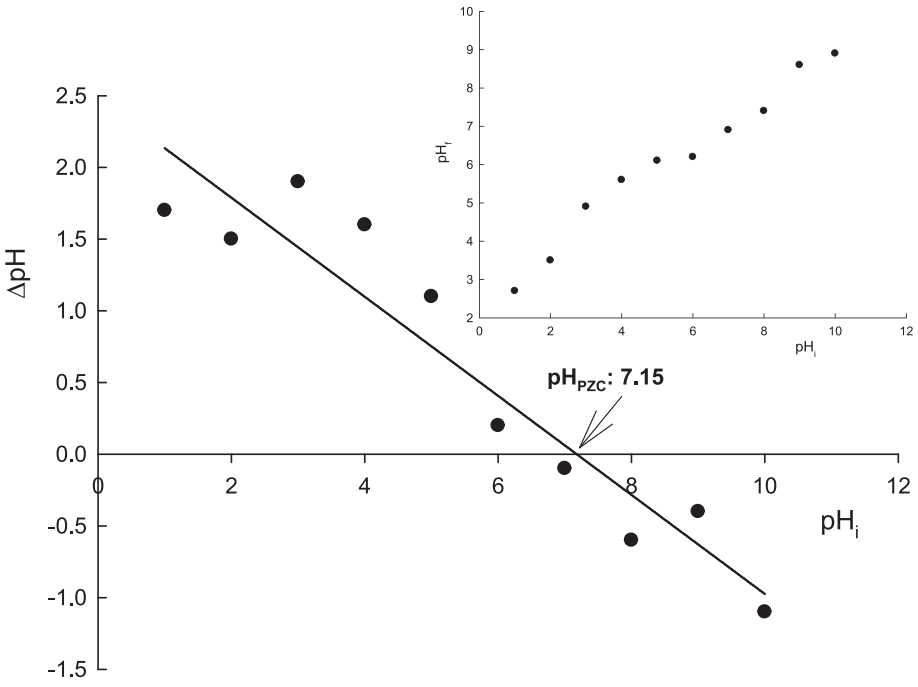

Fig. 7. PZC point of adsorbent.

3.1.5. Thermal stability

The TGA curves of Cs@Epic/Calcium apatites before and after Pb (II) adsorption are illustrated in Fig. 6. Below 200 °C, the composite exhibited excellent thermal stability, with the microspheres retaining 58.5 % of their initial weight when heated to 600 °C. The sharp weight loss observed at this temperature was attributed to the pyrolysis of the organic components of Chitosan.A fter the adsorption of Pb (II), an additional decomposition step appeared in the range of 50–100 °C, which could be linked to the desorption of residual water. It appeared that the thermal stability of the Pb (II)-loaded composite was slightly reduced. However, they still had a slightly higher residual weight of 54.8 % at 600 °C. This suggests that the interaction between the composite and Pb (II) led to the formation of a more stable complex, despite the impact on thermal stability.

3.2. Adsorption studies

3.2.1. The "Point of Zero Charge" for the adsorbent and the influence of pH on adsorption

Among the pivotal factors influencing adsorption, the solution's pH holds particular significance. The pH of the solution wields a tripartite influence on adsorption mechanisms. Primarily, it imparts an effect on

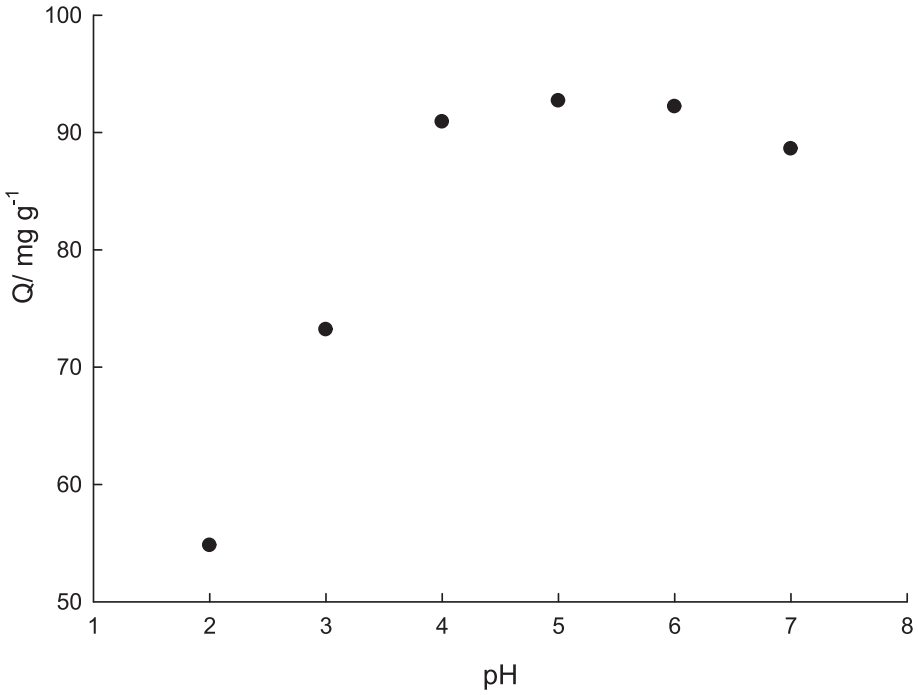

Fig. 8. pH effect on adsorption.

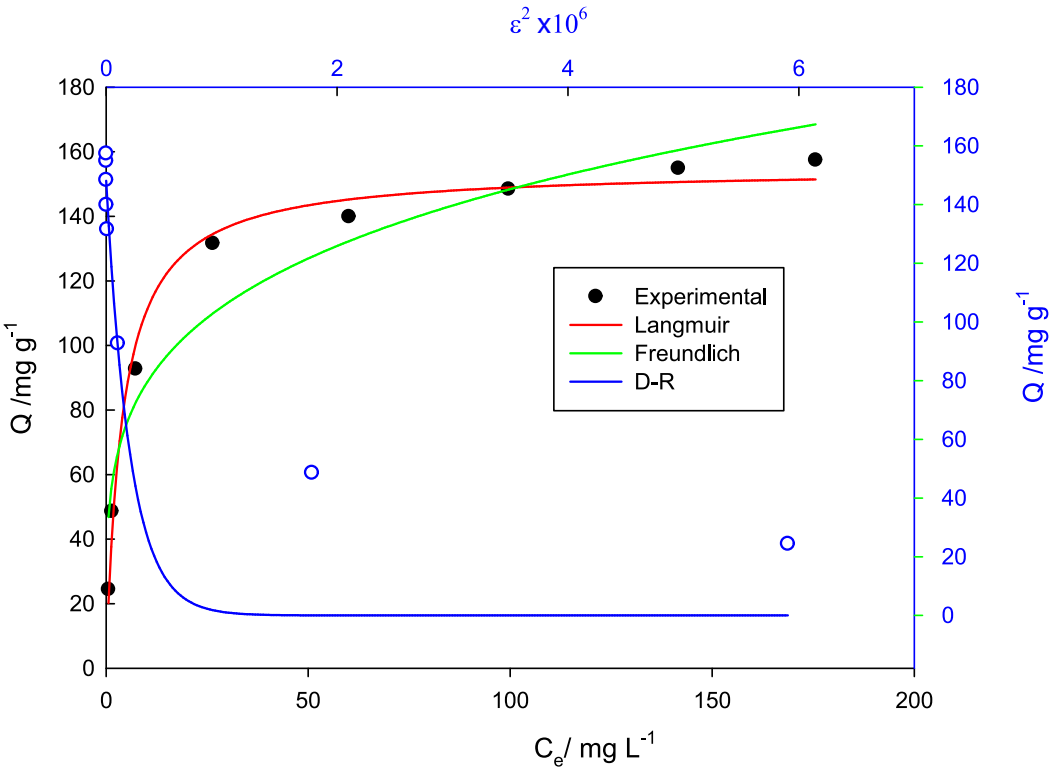

Fig. 9. Equilibrium isotherm parameters for Pb (II) uptake onto Cs@Epic/Calcium apatites.

the ion species' structure present within the solution, thereby dictating the prevailing species. Subsequently, by inducing alterations in the surface charge, it determines the prevailing mode of interaction between the solid and the solution, crucial for adsorption processes. The third facet encompasses the competition between species to be adsorbed, encompassing the contest between H^+ and OH^- ions, which can confer either favorable or adverse implications on the adsorption process.

Given the multifaceted impacts of pH, it emerges as a critical consideration to ascertain both the solution's pH and the surface pH at the liquid–solid interface to attain optimal adsorption outcomes. To this end, an initial assessment was conducted to determine the adsorbent's surface charge across various pH levels, with a consistent ionic strength. This analysis aimed to discern alterations in surface charge across diverse pH levels and to identify the Point of Zero Charge (PZC) [22], denoted in Fig. 7. The PZC, often referred to as the zero-charge point, was identified at 6.7. Consequently, this signifies that below this threshold, the dominant surface charge remains positive, while beyond this point, the prevailing charge transitions to a negative state.

Regarding the influence of pH on adsorption, a series of adsorption investigations were conducted, maintaining a constant lead concentration while varying the pH levels. The outcomes are depicted in Fig. 8. Notably, a subdued level of adsorption was observed at lower pH values.

Table 1
Comparison table various composites for Pb (II) adsorption.

Adsorbent	q_{max} (mg. g^{-1})	Reference
Fe3O4@TCA@CS nanocomposite	204.9	[24]
Poly-o-toluidine/stannic (IV) triethanolamine	17.85	[25]
ECCSB@Fe_3O_4	86.20	[26]
Chitosan/TiO_2	163.4	[27]
Magnetic chitosan/graphene oxide composite	121.3	[28]
Amino-thiol functionalized Chitosan	142.2	[29]
MOF in chitosan	397.3	[30]
Cs/Fap	60.24	[31]
Cs@Epic/Calcium apatites	154.88	This study

This trend can be attributed to the cationic nature of the surface under such conditions, leading to competition between lead ions and protons within the environment. This competition subsequently engenders a reduction in adsorption due to the intensified repulsive forces between the solid and the solution. Conversely, an upsurge in adsorption was evident with ascending pH values, reaching its zenith at the Point of Zero Charge (PZC) of the medium. The PZC represents a juncture where both positive and negative charges are distributed approximately uniformly across the surface. It's noteworthy that the study did not encompass alkaline conditions due to the potential presence of lead hydroxides, which could precipitate alongside the adsorption process under these circumstances.

3.2.2. *Lead concentration effect and adsorption parameters*

Adsorption parameters such as adsorption capacity, adsorption energy, and adsorbent surface properties are important for the process. For this purpose, a series of experiments were carried out to observe the behavior of adsorption at different adsorbate concentrations and to obtain parameters related to the process by investigating the fit of the results to various mathematical equations. For this purpose, adsorption models derived from various mathematical equations are used. Langmuir, Freundlich, and Dubinin Radushkevich models [23], which give frequent and accurate results, were used in the evaluation of isotherms in this study. For this purpose, to investigate the effect of lead ion concentration on adsorption, adsorption studies were carried out at different lead ion concentrations, constant temperature, and constant adsorption time and the experimental results and the fit curves of these results to the models are given in Fig. 9 and the parameters derived from these curves are given in Table 2.

Adsorption isotherm conforms to L-type isotherm in Giles classification. In this isotherm, adsorption occurs at a high rate at initial and small adsorbate concentrations, while adsorption centers are filled as the adsorbate concentration increases and a plateau is reached. The maximum adsorption amount found from the Langmuir model is given in Table 2. This model accepts the adsorbent surface as homogeneous

Table 2
Equilibrium adsorption parameters of Pb (II) on Cs@Epic/Calcium apatites.

Langmuir			Freundlich			D-R		
Q_{max}	K_L	R^2	a	β	R^2	Q_{DR}	K_{DR}	R^2
154.88	0.25	0,987	52.51	0.23	0.926	148.3	4.776×10^{-6}	0.824

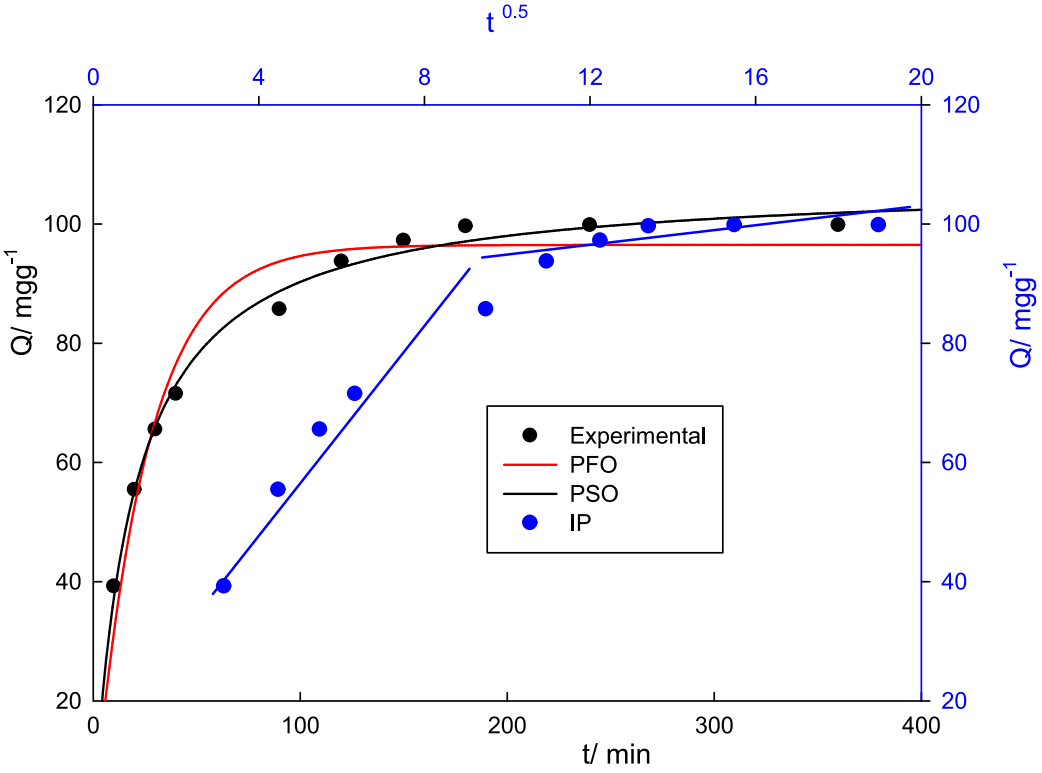

Fig. 10. Effect to f time to adsorption.

Table 3
Kinetic model parameters for Pb (II)adsorption.

	qe	q_M	k	r^2		
PFO	96.26	96.50	0.0395	0.954		
PSO	qe	q_M	k	r^2	H	$t^{1/2}$
	96.26	107.18	4.97×10^{-4}	0.993	5.71	18.78
			k	r^2		
IP			3.81	0.823		

and states that there are centers where adsorption takes place. The adsorption capacity found from the model was 158, 88 mgg^{-1}, which is a very high adsorption capacity. Freundlich model is used to determine the adsorbate surface heterogeneity [23]. The β value found here is considered a measure of surface heterogeneity. This value is between 0 and 1 and indicates the suitability of adsorption. If the value is >1, it means that the adsorption is not suitable. When compared with the lead adsorption capacities of similar adsorbents based on chitosan given in the table, it is seen that it has a very high adsorption capacity. Table 1: Pb (II) adsorption performance with other Cs-based adsorbents.

3.2.3. *Influence of time to adsorption and kinetic parameters*

To determine the kinetic parameters of adsorption, a series of experiments were carried out. The results of the experiments and the graph showing the fit of the theoretical models are given in Fig. 10 and the parameters found from the models used are given in Table 3. Considering the fit coefficients of the theoretical models pseudo-first-order (PFO), pseudo-second-order (PSO), and intraparticle diffusion (IP) [32], it is seen that adsorption can be explained by the PSO model. The PSO model generally assumes that adsorption occurs at small initial concentrations and through activity centers. The step that determines the rate of adsorption is determined by the transfer of ions to these adsorption centers. The kinetics of adsorption is quite complex and is formed by the occurrence of many consecutive events, such as surface transfer, surface film formation, and diffusion into pores [33]. Although the kinetics of these events during adsorption is different, it is the dominant type of adsorbent-adsorbate interaction that determines the kinetics of the whole process. Although many studies indicate that the appropriate model can be selected based on the fit coefficients of adsorption models to experimental values, this is not sufficient. The structure of the adsorbent and adsorption mechanism should be discussed for the selection of the kinetic model. The fit of the experimental results to the IP model was investigated and the fit curve is given in the figure. Although the R^2 value is not close to 1, the fact that it is multilinear indicates that adsorption occurs in two stages.

3.2.4. *Influence of temperature on adsorption and thermodynamic parameters*

To find the adsorption thermodynamic parameters, adsorption studies were carried out at different temperatures (298–308–318 K) and a constant lead concentration (100 ppm). The results are given in Fig. 11 and the parameters are given in Table 4. The results were calculated using Van't Hoff (reference) equation. The enthalpy of adsorption was found to be positive, i.e. energy consumption. Adsorption entropy was

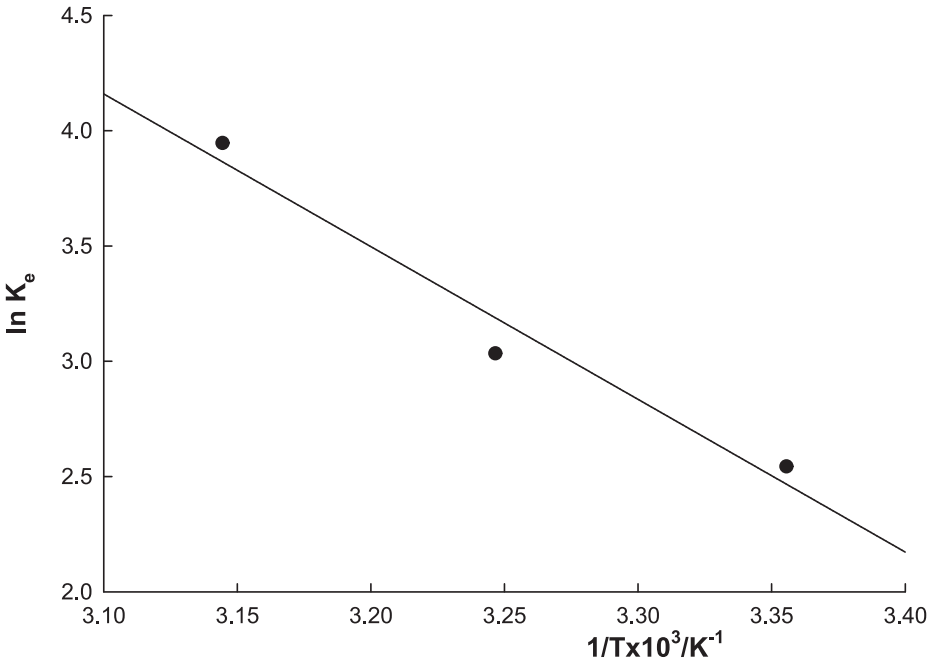

Fig. 11. Temperature effect on adsorption.

Table 4
Thermodynamic parameters.

Adsorbent	ΔH° (KJ/mol)	ΔS° (KJ/mol.K)	ΔG° (KJ/mol)		
			298 K	308 K	318 K
Cs@Cross/Hp	51,16	0,196	−6,30	−8,01	−10,16

found to be positive, i.e. an increase in disorders. This result is the entropy of the whole adsorption process. The increase in entropy in the whole process can be explained by the contribution of secondary events to entropy during the transition of metal ions in the solution to the solid surface. When the whole process such as dehydration of ions, ion exchange between the surface and the solution, and dissociation of water are evaluated together, entropy increase is observed. The free enthalpy of adsorption was found to be negative at all temperatures. This result shows that the adsorption process is spontaneous at all temperatures studied.

3.2.5. Effect of adsorbent dosage on adsorption

To investigate the effect of adsorbent amount on adsorption, an adsorption study was carried out using different amounts of adsorbent

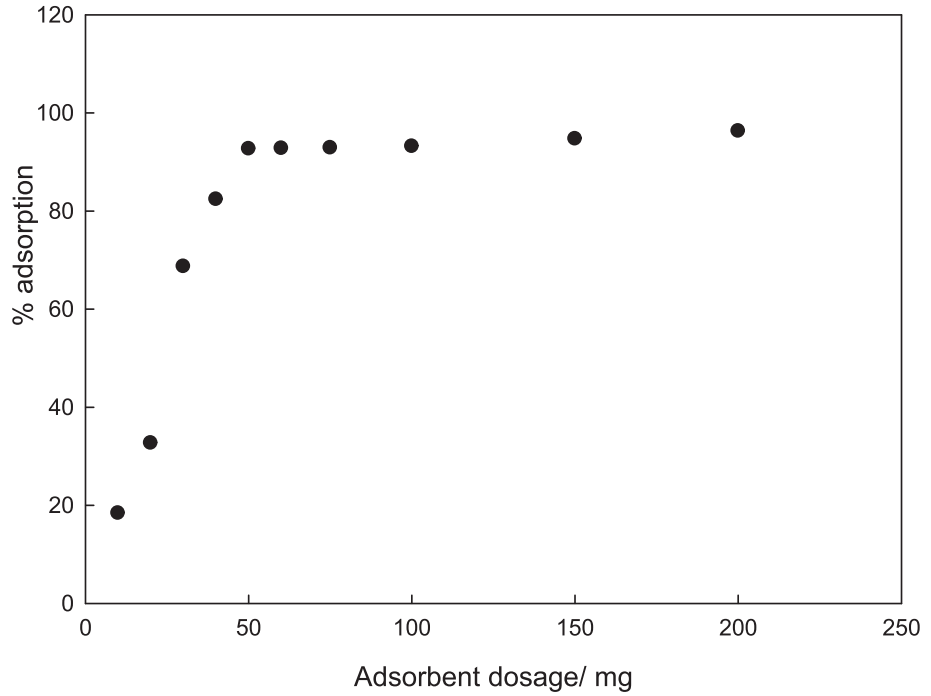

Fig. 12. Influence of adsorbent dosage on adsorption.

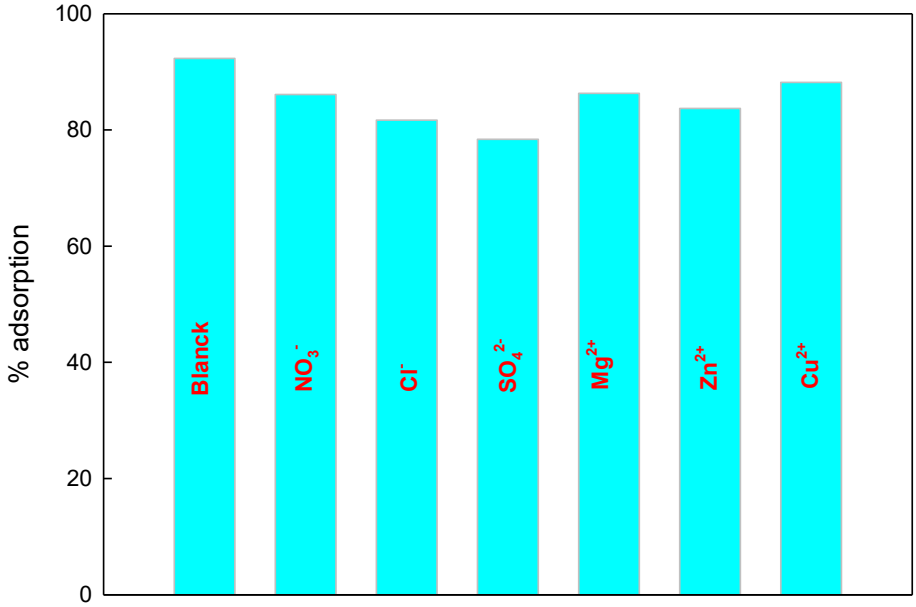

Fig. 13. Change of adsorption in the existence of co-ions.

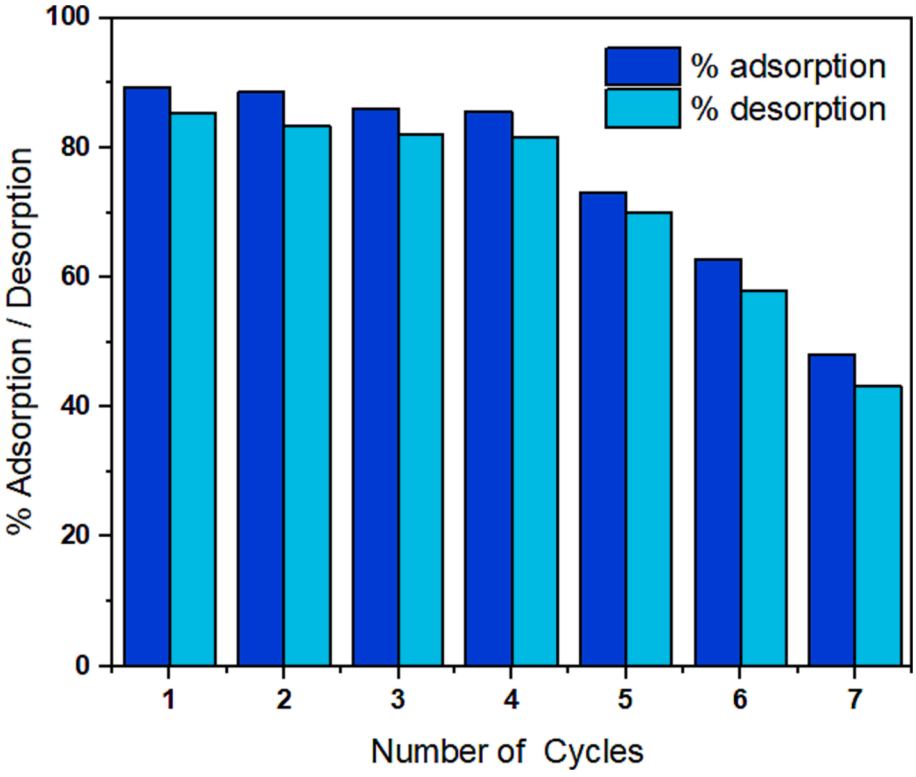

Fig. 14. Adsorption-desorption cycles for Pb (II) recovered.

mass with all other parameters constant, and the percentage adsorption values are given in Fig. 12. It can be seen that as the adsorbent amounts increase, adsorption also increases. This can be explained by the increase in adsorption centers with increasing adsorbent amounts. However, above a certain amount, the percentage adsorption value reaches a plateau. This value was found as 50 mg. Since the adsorption amounts above this did not change, this mass was taken in all other adsorption studies.

3.2.6. Effect of co-anions

To investigate the effect of secondary ions on adsorption, adsorption study was carried out in the presence of different ions and the results were given in Fig. 13. An adsorption study was carried out with a constant (100 ppm) concentration of lead and other ions. As seen in Fig. 13, adsorption reached the highest value only in the presence of la ead solution. A slight decrease in adsorption was observed in the presence of negatively charged ions. This can be explained by the fact that lead ions that cannot interact with the surface are not adsorbed as a result of the interaction of anions with lead. In the presence of cations, a competition

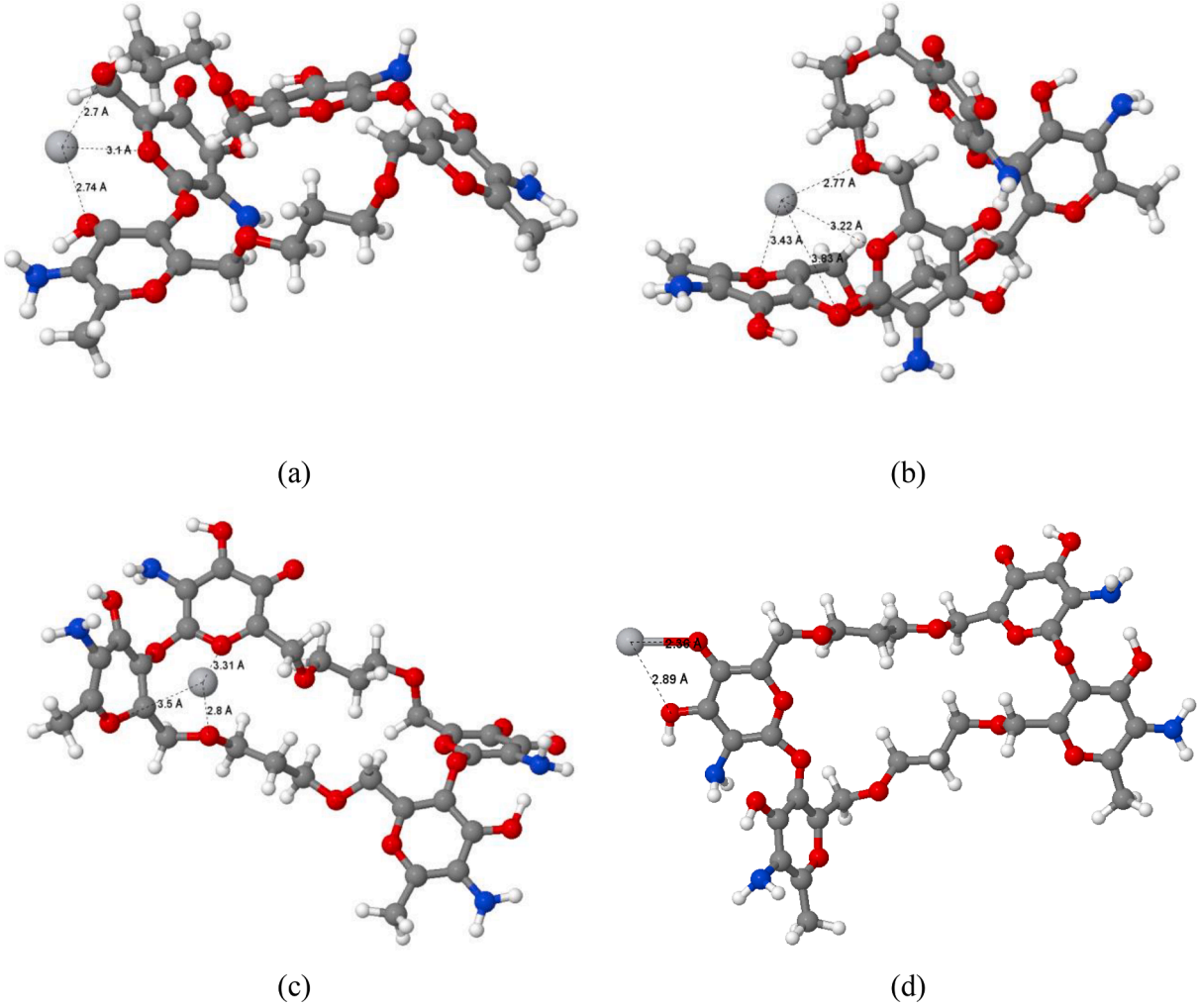

Fig. 15. Optimized geometries of four $C_{32}H_{38}N_4O_{16}Pb^{2+}$ complexes: complex 1 (a), complex 2 (b), complex 3 (c), and complex 4 (d).

between lead and cations can be mentioned. However, it is observed that this competition hdoes not affect adsorption.

3.2.7. *Regeneration study*

Regeneration studies were conducted over seven consecutive cycles (Fig. 14). It was observed that adsorption decreased from 86.3 % to 76.8 %, while desorption increased from 85 % to 71.2 % after four consecutive cycles. After the five cycles of regeneration, the adsorption performance of Cs@Epic/Calcium apatites gradually declined, reaching 46.5 % after seven consecutive regeneration cycles due to the reduction of active adsorption sites after repeated regeneration cycles. This study demonstrated that Cs@Epic/Calcium apatites were an excellent adsorbent that could be used for the removal and recovery of Pb (II) without significant loss in adsorbent performance.

4. Computational details

The $C_{32}H_{38}N_4O_{16}$ molecule and its complexes with Pb (II) ion; were fully optimized within the framework of the density functional theory with the exchange–correlation functional B3LYP [34,35] and the basis def2-SVP [36] implemented in the GAMESS [37] software. Grimme D3 corrections [38] were included for accurate accounting of possible noncovalent interactions between Pb (II) and adsorbent. Adsorption energy E_b was defined according to the formula

$$E_b = E(C_{32}H_{38}N_4O_{16}^0) + E(\text{Pb (II)}) - E(\text{complex}^{2+}).$$

Table 5
Calculated binding energies E_b (eV), frontier molecular orbitals HOMO and LUMO (eV), HOMO-LUMO gaps (eV), dipole moments D (Debye), and Pb–O distances l_{Pb-O} (Å) for four complexes of the $C_{32}H_{38}N_4O_{16}$ molecule with Pb (II) ion.

	E_b, eV	HOMO	LUMO	gap	D	l_{Pb-O}
$C_{32}H_{38}N_4O_{16}$	–	−2.65	−2.36	0.29	10.63	–
Complex 1	12.60	−8.97	−7.31	1.66	18.85	2.70; 2.74; 3.10
Complex 2	13.09	−9.25	−7.86	1.39	18.40	2.77; 3.22; 3.43; 3.83
Complex 3	11.98	−9.30	−7.72	1.59	17.90	2.80; 3.31; 3.50; 3.82
Complex 4	11.91	−7.02	−6.76	0.26	23.30	2.36; 2.89

Here $E(C_{32}H_{38}N_4O_{16}^0)$, E(Pb (II)) and $E(\text{complex}^{2+})$ are the total energies of the pristine molecule, lead ion, and their complex, respectively. Visualization was done with the JMol software [39].

5. Results

The adsorbent molecule contains many oxygen atoms that can adsorb lead ions. We selected and considered four configurations, which geometries are presented in Fig. 15a–d. The structure of the molecule ensures the placement of 2–4 oxygen atoms around the ion. Characteristics of four considered complexes are collected in Table 5. In all complexes, the binding energy is about 12 eV, indicating very strong

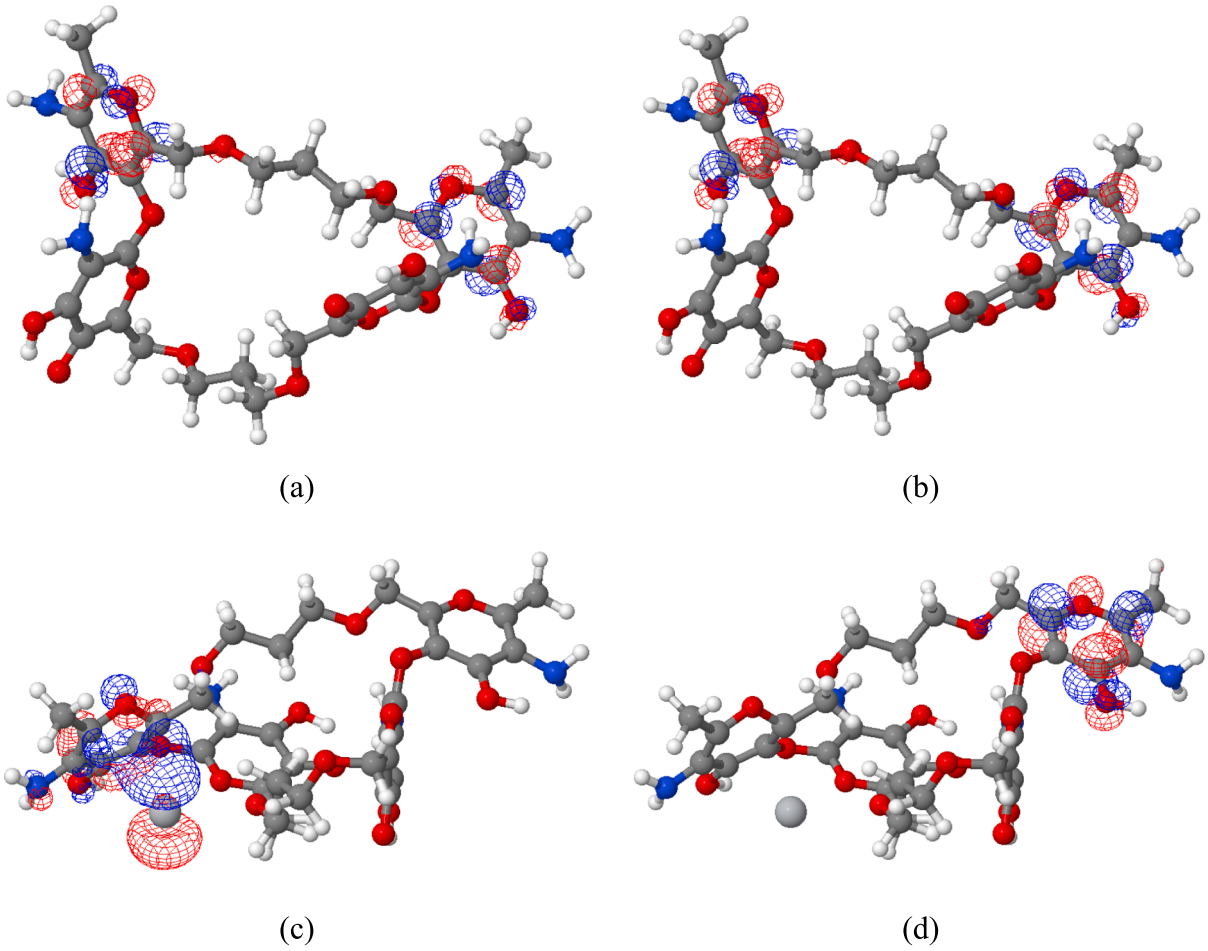

Fig. 16. Frontier orbitals HOMO (a) and LUMO (b) of the molecule $C_{32}H_{38}N_4O_{16}$. The same HOMO (c) and LUMO (d) orbitals of the most stable $C_{32}H_{38}N_4O_{16}Pb^{2+}$ complex (complex 2 in Table 1).

adsorption. The strongest interaction between the molecule and Pb (II) ion is achieved for complex 2, in which the ion is surrounded by four oxygen atoms. The formation of all complexes is associated with a sharp decrease in the energy of the boundary orbitals, which is mainly due to electrons transfer to the positively charged ion. As shown in Table 5, the first three complexes with the lowest energies have HOMO-LUMO gaps of about 1.5 eV, which are several times higher than the gap of the original molecule. Thus, the adsorption process can be easily detected by changing the optical properties of the system. The spatial structures of HOMO and LUMO orbitals of the pristine molecule and the most stable complex 2 are compared in Fig. 16. One can see that the adsorption results in the shifting of the HOMO orbital from the C_5O ring to the Pb (II) ion.

6. Conclusion

During this study, we demonstrated the synthesis of composites with significant specific surfaces using natural chitosan. XRD, SEM/EDS, FTIR, and TGA results confirmed the impregnation and penetration of calcium phosphates into the chitosan matrix.

The adsorption of Pb(II) by the composite was investigated in terms of time, pH, adsorbent mass, and initial adsorbate concentration. The adsorption isotherms of the studied metal ions on the mentioned composites exhibited a strong correlation with the Langmuir model, indicating monolayer adsorption with a maximum adsorption capacity (Qm) of 158.88 mg/g. The pseudo-second-order kinetic model was found to be the most suitable for describing the kinetics of lead adsorption. The highest adsorption capacity of the new materials was observed at the natural pH of lead ions.

Thermodynamic analysis ($\Delta G < 0$, $\Delta S > 0$, and $\Delta H > 0$) revealed that the adsorption process is feasible, spontaneous, and endothermic. Finally, regeneration tests demonstrated that the removal efficiency remained intact after four cycles, allowing for the reuse of these composites for water treatment purposes. This study underscores the potential of these composites as efficient adsorbents for the removal of Pb (II) from aqueous solutions.

CRediT authorship contribution statement

Rachid El Kaim Billah: Writing – original draft, Investigation, Writing – review & editing. **Selçuk Şimşek:** Conceptualization, Methodology, Supervision, Writing – original draft, Writing – review & editing. **Hicham Majdoubi:** Writing – original draft, Investigation. **Savaş Kaya:** Writing – original draft, Investigation, Writing – review & editing, Software. **Mahfoud Agunaou:** Writing – original draft, Investigation. **Abdessadik Soufiane:** Writing – original draft, Investigation. **Konstantin P. Katin:** Methodology, Writing – original draft, Software.

Declaration of Competing Interest

The authors declare that they have no known competing financial interests or personal relationships that could have appeared to influence the work reported in this paper.

Data availability

No data was used for the research described in the article.

Acknowledgments

The present study was partly supported by Sivas Cumhuriyet University Scientific Research Projects Commission. The authors have declared no conflict of interest.

References

[1] Nordberg GF, Fowler BA, Nordberg M, (Eds.), Handbook on the Toxicology of Metals, Academic Press, 2014.
[2] Lead poisoning: https://www.who.int/news-room/fact-sheets/detail/lead-poisoning-and-health, 31 August 2022, (accessed 18 July 2023).
[3] D. Lakherwal, Adsorption of heavy metals: a review, Int. J. Environ. Res. Dev. 4 (1) (2014) 41–48.
[4] S. Şimşek, E. Yılmaz, A. Boztuğ, Amine-modified maleic anhydride containing terpolymers for the adsorption of uranyl ion in aqueous solutions, J. Radioanal. Nucl. Chem. 298 (2013) 923–930.
[5] S. Şimşek, Y. Derin, S. Kaya, Z.M. Şenol, K.P. Katin, A. Özer, A. Tutar, High-performance material for the effective removal of uranyl ion from solution: computationally supported experimental studies, Langmuir 38 (33) (2022) 10098–10113.
[6] R.E.K. Billah, S. Kaya, S. Şimşek, E.M. Halim, M. Agunaou, A. Soufiane, Removal and regeneration of As (V) in aqueous solutions by adsorption on calcined fluorapatite, Int. J. Environ. Sci. Technol. (2022) 1–10.
[7] R. El Kaim Billah, I. Ayouch, Y. Abdellaoui, Z. Kassab, M.A. Khan, M. Agunaou, B. H. Jeon, A novel chitosan/nano-hydroxyapatite composite for the adsorptive removal of Cd (II) from aqueous solution, Polymers 15 (6) (2023), 1524.
[8] I.O. Saheed, W. Da Oh, F.B.M. Suah, Chitosan modifications for adsorption of pollutants–a review, J. Hazard. Mater. 408 (2021), 124889.
[9] S. Pai, S.M. Kini, R. Selvaraj, A. Pugazhendhi, A review of the synthesis of hydroxyapatite, its composites and adsorptive removal of pollutants from wastewater, J. Water Process Eng. 38 (2020), 101574.
[10] R.E.K. Billah, Z. Azoubi, E.A. López-Maldonado, H. Majdoubi, H. Lgaz, E.C. Lima, R. Jugade, Multifunctional cross-linked shrimp waste-derived chitosan/MgAl-LDH composite for removal of As (V) from wastewater and antibacterial activity, ACS omega 8 (11) (2023) 10051–10061.
[11] R.E. Billah, Y.H. Kaim, M.A. Otman Goudali, S. Abdessadik, Removal and regeneration of iron (III) from water using new treated fluorapatite extracted from natural phosphate as adsorbent, Biointerface Res. Appl. Chem 11 (2021) 13130–13140.
[12] O. Goudali, R. El Kaimbillah, M. Agunaou, M. El Azhar, A. Soufiane, Comparative study of adsorption of fluoride ions on chitosan gel beads and cross-linked chitosan gel beads, Egypt. J. Chem. 63 (2020) 4253–4259, https://doi.org/10.21608/ejchem.2019.12621.1795.
[13] R.E.K. Billah, M.A. Islam, H. Lgaz, E.C. Lima, Y. Abdellaoui, Y. Rakhila, O. Goudali, H. Majdoubi, A.A. Alrashdi, M. Agunaou, A. Soufiane, Shellfish waste-derived mesoporous chitosan for impressive removal of arsenic(V) from aqueoussolutions: a combined experimental and computational approach, Arab. J. Chem. (2022), 104123, https://doi.org/10.1016/j.arabjc.2022.104123.
[14] E.L.R. Kaim Billah, A. Zaghloul, H.A. Ahsaine, A. BaQais, I. Khadoudi, N. El Messaoudi, M. Agunaou, A. Soufiane, R. Jugade, Methyl orange adsorption studies on glutaraldehyde cross-linking chitosan/fluorapatite-based natural phosphate composite, Int. J. Environ. Anal. Chem. (2022) 1–17, https://doi.org/10.1080/03067319.2022.2130690.
[15] B.R. El Kaim, F. El Bachraoui, B. El Ibrahimi, et al., Mechanistic understanding of Nickel(II) adsorption onto fuorapatite-based natural phosphate via Rietveld refnement combined with Monte Carlo simulations, J Solid State Chem 310 (2022), 123023, https://doi.org/10.1016/j.jssc.2022.123023.
[16] R.E.K. Billah, M.A. Khan, Y.-K. Park, et al., A comparative study on hexavalent chromium adsorption onto chitosan and chitosan-based composites, Polymers 13 (2021), 3427, https://doi.org/10.3390/polym13193427.
[17] W.S. Wan Ngah, M.A.K.M. Hanafiah, S.S. Yong, Adsorption of humic acid from aqueous solutions on crosslinked chitosan–epichlorohydrin beads: kinetics and isotherm studies, Colloids Surf. B: Biointerfaces 65 (1) (2008) 18–24, https://doi.org/10.1016/j.colsurfb.2008.02.00.
[18] V.B. Gavalyan, Synthesis and characterization of new chitosan-based Schiff base compounds, Carbohydr. Polym. 145 (2016) 37–47, https://doi.org/10.1016/j.carbpol.2016.02.076.
[19] H.A. Said, H. Noukrati, H. Ben Youcef, A. Bayoussef, H. Oudadesse, A. Barroug, Mechanical behavior of hydroxyapatite-chitosan composite: effect of processing parameters, Minerals 11 (2021), 213, https://doi.org/10.3390/min11020213.
[20] K.S. Sing, R.T. Williams, Physisorption hysteresis loops and the characterization of nanoporous materials, Adsorpt. Sci. Technol. 22 (2004) 773–782.
[21] M. Thommes, K. Kaneko, A.V. Neimark, J.P. Olivier, F. Rodriguez-Reinoso, J. Rouquerol, K.S.W. Sing, Physisorption of gases, with special reference to the evaluation of surface area and pore size distribution (IUPAC Technical Report), Pure Appl. Chem. (2015), https://doi.org/10.1515/pac-2014-1117.
[22] N. Fiol, I. Villaescusa, Determination of sorbent point zero charge: usefulness in sorption studies, Environ. Chem. Lett. 7 (2009) 79–84.
[23] N. Ayawei, A.N. Ebelegi, D. Wankasi, Modelling and interpretation of adsorption isotherms, J. Chem. (2017).
[24] M. Algamdi, A. Alshahrani, M. Alsuhybani, Chitosan grafted tetracarboxylic functionalized magnetic nanoparticles for removal of Pb (II) from an aqueous environment, Int. J. Biol. Macromol. 225 (2023) 1517–1528.
[25] E.A. Abdelrahman, R.M. Hegazey, Utilization of waste aluminum cans in the fabrication of hydroxysodalite nanoparticles and their chitosan biopolymer composites for the removal of Ni(II) and Pb (II) ions from aqueous solutions: kinetic, equilibrium, and reusability studies, Microchem. J. 145 (2019) 18–25, https://doi.org/10.1016/j.microc.2018.10.016.
[26] Y. Yan, G. Yuvaraja, C. Liu, L. Kong, K. Guo, G.M. Reddy, G.V. Zyryanov, Removal of Pb(II) ions from aqueous media using epichlorohydrin crosslinked chitosan Schiff's base@Fe3O4 (ECCSB@Fe3O4), Int. J. Biol. Macromol. 117 (2018) 1305–1313, https://doi.org/10.1016/j.ijbiomac.2018.05.204.
[27] Y. Tao, L. Ye, J. Pan, Y. Wang, B. Tang, Removal of Pb(II) from aqueous solution on chitosan/TiO2 hybrid film, J. Hazard. Mater. 161 (2009) 718–722, https://doi.org/10.1016/j.jhazmat.2008.04.012.
[28] M.S. Samuel, S.S. Shah, J. Bhattacharya, K. Subramaniam, N.D. Pradeep Singh, Adsorption of Pb(II) from aqueous solution using a magnetic chitosan/graphene oxide composite and its toxicity studies, Int. J. Biol. Macromol. 115 (2018) 1142–1150, https://doi.org/10.1016/j.ijbiomac.2018.04.185.
[29] J.S. Alnawmasi, Construction of amino-thiol functionalized ion-imprinted chitosan for lead (II) ion removal, Carbohydr. Polym. 308 (2023), 120596.
[30] Y. Ma, D. You, Y. Fang, J. Luo, Q. Pan, Y. Liu, W. Yang, Confined growth of MOF in chitosan matrix for removal of trace Pb (II) from reclaimed water, Sep. Purif. Technol. 294 (2022), 121223.
[31] R. El KaimBillah, M.A. Islam, M. Agunaou, A. Soufiane, A promising chitosan/fluorapatite composite for efficient removal of lead (II) from an aqueous solution, Arab. J. Geosci. 14 (2021) 1134, https://doi.org/10.1007/s12517-021-07473-w.
[32] M. Benjelloun, Y. Miyah, G.A. Evrendilek, F. Zerrouq, S. Lairini, Recent advances in adsorption kinetic models: their application to dye types, Arab. J. Chem. 14 (4) (2021), 103031.
[33] H. Qiu, L. Lv, B.C. Pan, Q.J. Zhang, W.M. Zhang, Q.X. Zhang, Critical review in adsorption kinetic models, J. Zhejiang Univ.-Sci. A 10 (5) (2009) 716–724.
[34] A.D. Becke, Density-functional thermochemistry. III. The role of exact exchange, J. Chem. Phys. 98 (7) (1993) 5648–5652, https://doi.org/10.1063/1.462066.
[35] C. Lee, W. Yang, R.G. Parr, Development of the Colle-Salvetti correlation-energy formula into a functional of the electron density, Phys. Rev. B 37 (2) (1988) 785–789, https://doi.org/10.1103/PhysRevB.37.785.
[36] F. Weigend, R. Ahlrichs, Balanced basis sets of split valence, triple zeta valence and quadruple zeta valence quality for H to Rn: design and assessment of accuracy, Phys. Chem. Chem. Phys. 7 (2005) 3297, https://doi.org/10.1039/b508541a.
[37] G.M.J. Barca, C. Bertoni, L. Carrington, D. Datta, N. De Silva, J.E. Deustua, D.G. Fedorov, J.R. Gour, A.O. Gunina, E. Guidez, T. Harville, S. Irle, J. Ivanic, K. Kowalski, S.S. Leang, H. Li, W. Li, J.J. Lutz, I. Magoulas, J. Mato, V. Mironov, H. Nakata, B.Q. Pham, P. Piecuch, D. Poole, S.R. Pruitt, A.P. Rendell, L.B. Roskop, K. Ruedenberg, T. Sattasathuchana, M.W. Schmidt, J. Shen, L. Slipchenko, M. Sosonkina, V. Sundriyal, A. Tiwari, J.L. Galvez Vallejo, B. Westheimer, M. Włoch, P. Xu, F. Zahariev, M.S. Gordon, Recent developments in the general atomic and molecular electronic structure system, J. Chem. Phys. 152 (2020) 154102, doi: 10.1063/5.0005188.
[38] S. Grimme, J. Antony, S. Ehrlich, H. Krieg, A consistent and accurate ab initio parametrization of density functional dispersion correction (DFT-D) for the 94 elements H-Pu, J. Chem. Phys. 132 (2010), 154104, https://doi.org/10.1063/1.3382344.
[39] V.F. Scalfani, A.J. Williams, V. Tkachenko, K. Karapetyan, A. Pshenichnov, R. M. Hanson, J.M. Liddie, J.E. Bara, Programmatic conversion of crystal structures into 3D printable files using Jmol, J. Cheminform. 8 (2016) 66, https://doi.org/10.1186/s13321-016-0181-z.